FACTA UNIVERSITATIS (NIŠ)
SER.: ELEC. ENERG. vol. 22, no. 1, December 2009, 341-360

Assessment of Unsymmetrical Voltage Sag Effectson AC Adjustable Speed Drives

Milutin Petronijević, Nebojša Mitrović, Vojkan Kostić, and Borislav Jeftenić

Abstract: This paper analyses the influence of unsymmetrical voltage sags on the increase of torque and speed deviation induction motor adjustable speed drives. The three following general types of induction motor drives control are analysed: scalar-controlled (V/Hz), rotor-field-oriented (RFO) and direct-torque-controlled (DTC). The analytical expression for variations of dc link voltage incorporated into the corresponding drive models and formulas for assessment of current/torque deviation are derived depending on the applied control algorithm. Afterwards, the presented theoretical results for the deterioration of motor drive performance due to voltage sags are validated experimentally. Measurements of sag-caused mechanical vibrations are used for the additional verification of the obtained results.

Keywords: Power quality, voltage sag, induction motor drives, speed and torque deviation.

1 Introduction

VOLTAGE sags (dips) are power quality problems with the most often appearances in public power supply network. Sensitivity of adjustable speed drives (ASDs) to voltage sags was a subject of numerous studies and experimental researches (e.g. [1]). In continuous process applications, stop electric drives may occur due to deviations in the speed and/or electromagnetic torque. Majority of the previous works was, concentrated only on determining sensitivity limits related

Manuscript received on June 22, 2009.

M. Petronijević, N. Mitrović, and V. Kostić are with Faculty of Electronic Engineering, University of Niš, A. Medvedeva 14, 18 000 Niš, Serbia (e-mails: [milutin.petronijevic; nebojsa.mitrovic; vojkan.kostic]@elfak.ni.ac.rs). B. Jeftenić is with Faculty of Electrical Engineering, University of Belgrade, K. Alaksandra 73, 11 000 Belgrade, Serbia (e-mail: jeftenic@etf.rs).

to disconnection/tripping of analysed or tested ASDs due to the activation of their overcurrent/undervoltage protection systems.

The paper researches behaviour of scalar controlled (V/Hz), rotor field oriented (RFO) and direct torque controlled (DTC) induction motor (IM) drives in speed and torque controlled application in voltage sags circumstances. Analytical results, presented in this paper, show differences in behaviour of electrical drives, depending on the applied control algorithm, and suggest opportunities for improvement in practical applications.

The recent researches in ASD sag sensitivity did not take into account type and actual settings of applied drive control, and this paper aims to fill this gap by presenting corresponding analytical relations and experimental results for dc link voltage ripple, torque ripple and mechanical vibrations caused by unbalanced voltage sags. The use of experimental measurements was particularly important for the verification of the developed models and control algorithms of high-performance ASDs, as these are very complex. The presented results show that classical DTC drives using torque and flux comparators practically insensible to an increase of dc voltage ripple, while RFO-controlled drives and DTC drives with PI regulators for flux and torque control are only slightly sensible.

Section II of this paper provides a short description of single-line-to-ground faults caused voltage sags and analytically describes their consequences on dc link voltage deviation. Section III presents three analysed general control methods: scalar control (V/Hz), direct torque control (DTC) and rotor flux oriented (RFO) control. Section IV analytically compares influence of unbalanced voltage sags on ASD performance, and points out main differences in responses of ASDs with different controls. Based on the analysis of obtained analytical results, in this section also discusses and highlights key parameters and characteristics of ASDs affected by voltage sags. Finally, the last section of the paper presents some experimental results, including vibration spectra, for sag-caused torque harmonics.

2 Voltage Sags effects

Unbalanced voltage sags are of particular importance during the assessment of equipment sensitivity, as they are usually caused by single-line-to-ground faults (SLGFs), which are the most frequent types of system fault (responsible for around 70% of all faults, [2]). As one or two-phase voltages of SLGF-caused unbalanced single-phase and two-phase voltage sags are either unaffected, or with only a minor reduction in magnitude. During sag, ASD dc link voltage may, depending on the magnitude and duration of the experienced unbalanced sags, remain above the undervoltage protection limit. Numerous measurements around the world ([3]) point

to the fact that the expected value of the remaining voltage during the sags is closer to the upper limit (between 50% and 90% of nominal voltage). Frequency converter of the some manufacturer will not lead to failure, but it will certainly lead to performance deterioration. Figure 1 illustrates the distribution of the voltage sags and also refers to the fact that they usually last for a few seconds.

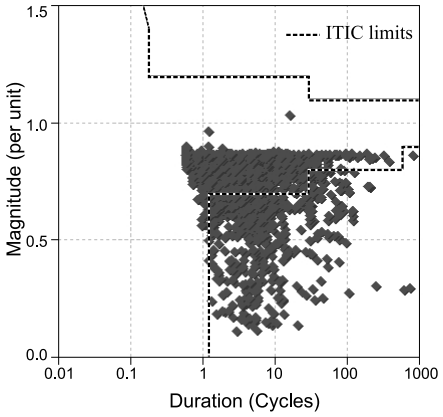

Fig. 1. Magnitude/duration chart of voltage sags (adopted from www.i-grid.com [3]).

Based on [2] it is known that SLGF's can produce B type sags with the depth in range of h=0 ... 1, while C and D types voltage sags depths are in range h=0.333...1. Phase voltage equations in complex form and the appropriate phasor diagrams that illustrate the above basic unsymmetrical sag types were given in Table 1. In this paper, the analysis was conducted precisely for these types of voltage sags, although similar conclusions can be drawn for the case of other types, but in case of voltage unbalance.

In case of B, C or D voltage sag input rectifier passes into single phase operations with the consequences as input current distortion and DC voltage ripple increase with dominant component at 100Hz and with average voltage reduction in C type voltage sag case. DC bus voltage $v_{dc}(t)$ in case of a voltage sag supply conditions, having in mind [4] is presented as:

$$v_{dc}(t) = V_{DC} + V_{DC2}\cos(2\omega_i t + \theta_2) \tag{1}$$

where V_{DC} presents an average voltage value, V_{DC2} is the second voltage harmonic, ω_i is power supply angular frequency ($2\pi 50s^{-1}$ or $2\pi 60\text{s}^{-1}$) and θ_2 is an appropriate angle of the second harmonic component referring to d-axis which defines point on wave at sag initiation. In general case, modulation signals can be represented:

$$u_i(t) = u_i^*(t) + e(t) \tag{2}$$

Table 1. Basic types of unsymmetrical voltage sags.

Sag type	Phasor diagram solid lines during fault	Phase-to-neutral voltages (*h* designates remain voltage in p.u.)
B	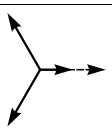	$U_a = hU$ $U_b = -(1/2)U - j(\sqrt{3}/2)U$ $U_c = -(1/2)U + j(\sqrt{3}/2)U$
C	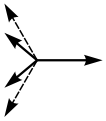	$U_a = U$ $U_b = -(1/2)U - j(\sqrt{3}/2)hU$ $U_c = -(1/2)U + j(\sqrt{3}/2)hU$
D	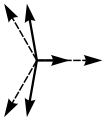	$U_a = hU$ $U_b = -(1/2)hU - j(\sqrt{3}/2)U$ $U_c = -(1/2)hU + j(\sqrt{3}/2)U$

where *e(t)* is injected harmonic (also represents direct transformation SV-PWM into carrier based PWM), and $u_i(t)$ are called fundamental signals for appropriate phase voltages (*i*=*a*, *b*, *c*). Fundamental components of line to neutral output PWM voltages are:

$$u_{an}(t) = \frac{1}{2}v_{dc}(t)[m \cdot \cos(\omega_s t + \varphi) + e_i(t)]$$
$$u_{bn}(t) = \frac{1}{2}v_{dc}(t)[m \cdot \cos(\omega_s t - \frac{2\pi}{3} + \varphi) + e_i(t)]$$
$$u_{cn}(t) = \frac{1}{2}v_{dc}(t)[m \cdot \cos(\omega_s t + \frac{2\pi}{3} + \varphi) + e_i(t)]$$

where ω_s - inverter output fundamental frequency with modulation index *m*. Phase angle φ corresponds to initial phase voltage angle related to *d* axis.

Combining equations (2) and (3), and applying coordinate transformations, induction motor stator voltages in *dq* reference frame that rotates at a synchronous reference speed ω_s, are:

$$u_{ds}(t) = \frac{1}{2}m[V_{DC}\cos\varphi + V_{DC2}\cos(2\omega_i t + \theta_2)\cos\varphi]$$
$$u_{qs}(t) = \frac{1}{2}m[V_{DC}\sin\varphi + V_{DC2}\cos(2\omega_i t + \theta_2)\sin\varphi]. \quad (3)$$

In equations above the second term is a direct consequence of dc link voltage ripple because of rectifier single-phase operation. Voltages given by equation (3) correspond to three-phase voltages with terms ω_s, $2\omega_i+\omega_s$ and $-2\omega_i+\omega_s$.

3 Description of Implemented ASD Models

Modern ASDs usually allow end-users to apply different types of control, as most manufacturers provide options for selecting different control methods in the same ASD. General classification divides induction motor controls into scalar-based and vector-based ([5]). The most commonly used control method in industry is a simple scalar-control, also known as constant Voltage/Frequency (V/Hz) control. Although very simple, V/Hz control is usually not implemented in high performance drive applications due to its drawbacks.

Opposite to scalar control, which allows for control of only output voltage magnitude and frequency, vector-based control methods enable control of instantaneous voltage, current and flux vectors. Accordingly, vector-based control algorithms result in significantly improved regulation of drive's dynamic characteristics and better sag ride-through capabilities. This is discussed in more detail in the next subsections.

3.1 V/Hz controlled ASDs

Numerous industrial and other applications with induction motors require control of motor speed (e.g., various paper, textile and material processing lines, fans, blowers, HVAC-heating, ventilation and air conditioning, etc.). As mentioned previously, V/Hz control is commonly selected as an optimal solution, because of its simplicity and low cost. Generally, V/Hz control can be realized as open-loop or closed-loop control, with the information on actual motor speed supplied to the controller in the latter case.

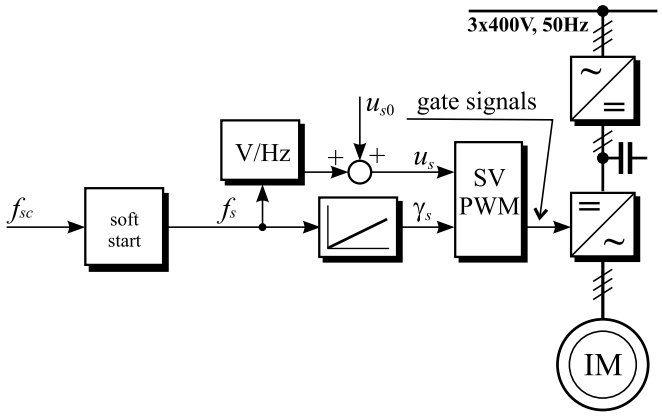

Fig. 2. Basic V/Hz control scheme.

The V/Hz control can be modified to offset the voltage drop across the inverter and stator resistance, which usually has a significant impact at low output frequencies/speeds. Algorithms implemented in practice may also include a dead-time compensation circuit and a torque estimator based on the measurement of stator currents and voltages, instead of using torque sensor. Figure 2 illustrates V/Hz open-loop control structure, where pulse-width modulation (PWM) is realised applying space vector technique (SVPWM) and output voltage fundamental component amplitude controlled according to:

$$u_s^* = u_{s0} + \frac{U_{sn}}{f_{sn}} f_s^* \tag{4}$$

where U_{sn} and f_{sn} are nominal voltage magnitude and frequency, u_{s0} – voltage offset (voltage drop compensation) and f_s^* designates output frequency reference value.

3.2 Rotor field oriented control of ASDs

Rotor-flux-oriented (RFO) vector control technique is dominant in modern high-performance ASDs. In this case, decoupled control of torque and rotor flux is achieved by acting on q and d stator current components, respectively, assuming that the reference frame is attached to rotor flux vector. One of the main features

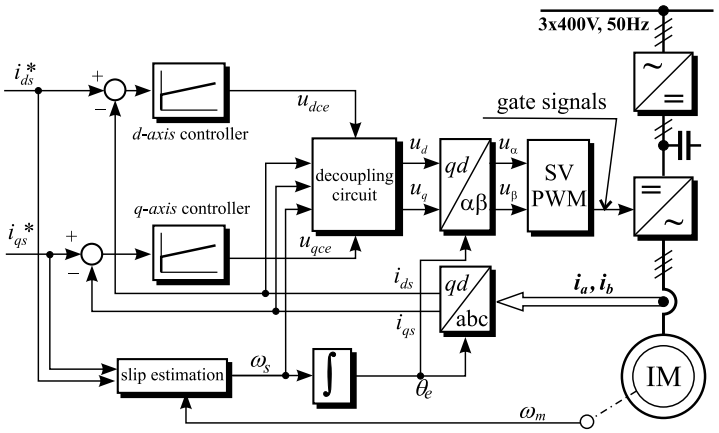

Fig. 3. Indirect RFO control scheme.

of the RFO control method is the application of the co-ordinate transformation. Stator currents are measured in a stationary coordinate frame, and the corresponding current components i_{sd} and i_{sq} are obtained by rotational transformation, using feed-forward estimator. Basic control structure of indirect RFO control (IFOC) is

illustrated in Fig. 3. Two inner PI controlled current loops for d and q stator current components are shown, as well as synchronous speed estimator (ω_s, based on reference stator currents components).

3.3 Direct torque control of ASDs

The notion of direct torque and flux control suggests the fact that instantaneous torque and flux values are controlled directly by appropriate switching states of the inverter. In the basic version, direct torque control (DTC) consists of a three-level hysteresis comparator for torque control and a two-level hysteresis comparator for flux control. The main problem in classical direct-torque-controlled ASD application is a high value of the torque ripple, which can be minimised by reducing calculation time for the switching states [6], or by using switching table modification [7]. In this paper, modified DTC scheme is used, in which α-β plane is divided into twelve sectors (denoted as "C12DTC"), instead in just six sectors, Fig. 4. This approach usually results in low/acceptable torque ripple and low distortion of stator currents.

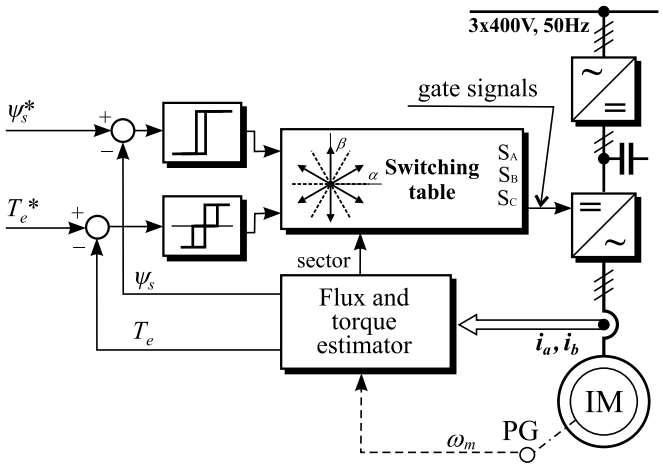

Fig. 4. Twelve sector DTC control scheme.

One of the favourable solutions for constant switching frequency and low torque ripple is described in [8] and illustrated in Fig. 5. This control scheme, designated as PIDTC, uses two PI controllers, one for flux control and the other for torque control.

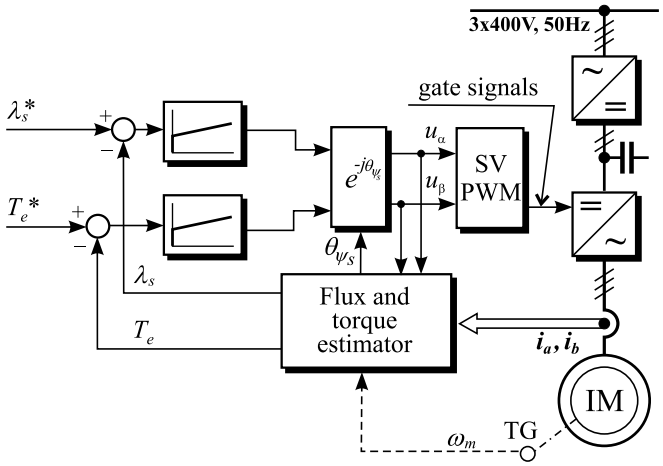

Fig. 5. PIDTC control scheme.

4 Theoretical Analysis and ASD Behavior Comparisons

Assuming magnetic linearity, the equivalent two-phase model of the symmetrical IM, represented in the synchronous rotating reference frame, is:

$$u_{ds} = R_s i_{ds} - \omega_s \psi_{qs} + \frac{\mathrm{d}}{\mathrm{d}t}\psi_{ds} \tag{5}$$

$$u_{qs} = R_s i_{qs} + \omega_s \psi_{ds} + \frac{\mathrm{d}}{\mathrm{d}t}\psi_{qs} \tag{6}$$

$$0 = R_r i_{dr} - (\omega_s - \omega_m)\psi_{qr} + \frac{\mathrm{d}}{\mathrm{d}t}\psi_{dr} \tag{7}$$

$$0 = R_r i_{qr} + (\omega_s - \omega_m)\psi_{dr} + \frac{\mathrm{d}}{\mathrm{d}t}\psi_{qr} \tag{8}$$

The relations between *dq* flux linkage and currents are:

$$\begin{aligned} \psi_{ds} &= L_s i_{ds} + M i_{dr}, \psi_{qs} = L_s i_{qs} + M i_{qr} \\ \psi_{dr} &= L_r i_{dr} + M i_{ds}, \psi_{qr} = L_r i_{qr} + M i_{qs} \end{aligned} \tag{9}$$

Electromagnetic torque can be calculated using the following formula:

$$T_e = 1.5P(M/L_r)(i_{qs}\psi_{dr} - i_{ds}\psi_{qr}). \tag{10}$$

In steady state condition, solving equations (6) - (9) in case of voltage given by equations (4), and applying the superposition theorem, we obtain expressions for

the *dq* stator currents:

$$i_{ds} = i_{ds0} + I_{ds2}\cos(2\omega_i t + \delta_{ds}) \tag{11}$$
$$i_{qs} = i_{qs0} + I_{qs2}\cos(2\omega_i t + \delta_{qs}), \tag{12}$$

where average stator current components are given by:

$$i_{ds0} = K_0\left[g_0\cos\varphi - b_0\sin\varphi\right], \quad \text{and}$$
$$i_{qs0} = K_0\left[g_0\sin\varphi + b_0\cos\varphi\right].$$

Magnitudes of additional oscillatory stator current components are (for simplicity it will be θ_2=0):

$$I_{ds2} = K_1\sqrt{|y_1|^2 + |y_2|^2 + 2|y_1||y_2|\cos(2\varphi + \angle y_1 + \angle y_2)} \tag{13}$$
$$I_{qs2} = K_1\sqrt{|y_1|^2 + |y_2|^2 + 2|y_1||y_2|\cos(2\varphi + \angle y_1 + \pi - \angle y_2)} \tag{14}$$

The values of certain coefficients in the previous equations are:

$$K_0 = \frac{1}{2}mV_{DC},\ K_1 = \frac{1}{4}mV_{DC2}$$
$$y_0 = g_0 + jb_0 = [r_s + j\omega_s L_{ls} + \{j\omega_s M \,\|\, (r_r/s_0 + j\omega_s L_{lr})\}]^{-1}$$
$$y_1 = [r_s + j\omega_1 L_{ls} + \{j\omega_1 M \,\|\, (r_r/s_1 + j\omega_1 L_{lr})\}]^{-1}$$
$$y_2 = [r_s + j\omega_2 L_{ls} + \{j\omega_2 M \,\|\, (r_r/s_2 + j\omega_2 L_{lr})\}]^{-1}$$
$$\omega_1 = 2\omega_i + \omega_s,\ \omega_2 = -2\omega_i + \omega_s,$$
$$s_0 = \frac{\omega_s - \omega}{\omega_s},\ s_1 = \frac{\omega_1 - \omega}{\omega_1},\ s_2 = \frac{\omega_2 - \omega}{\omega_2},$$

where ω denotes motor rotor angular speed, δ_{ds} and δ_{qs} represents second harmonic stator current components angle respect to *d* and *q* axis, respectively.

After combining (12) and (13), taking into account expressions (11), the torque value can be calculated in the closed form:

$$T_e = T_{e0} + T_{e2}\cos(2\omega_i t + \phi_2) + T_{e4}\cos(4\omega_i t + \phi_4), \tag{15}$$

where T_{e0} represents average torque value, T_{e2} represents the second harmonic component and T_{e4} represents the fourth harmonic components.

In the following chapters will be given the discussions on the impact of individual torque and current components, depending on the applied type of ASDs control.

4.1 DC link voltage reduction effects

Limitations, as a consequence of the maximum output current (I_{max}) and maximum output voltage (U_{max}) of an AC/DC converter, can be presented in the appropriate stator variable through the equations:

$$i_{qs}^2 + i_{ds}^2 \leq I_{\max}^2, \quad \text{and} \tag{16}$$

$$u_{qs}^2 + u_{ds}^2 \leq U_{\max}^2 \tag{17}$$

Maximum output current is determined by maximum continuous current of inverter semiconductor switches or induction motor rated current, i.e. maximum allowable thermal capacity of the converter or induction motor. The maximum stator voltage depends on the available DC-link voltage *vDC* and pulsewidth modulation (PWM) strategy ([9]).

Equation (18), in steady state and voltage limit condition, having in mind the relationships (6)-(11), can be written as:

$$A\, i_{ds}^2 + C\, i_{qs}^2 + B\, i_{ds}\, i_{qs} \leq U_{\max}^2 \tag{18}$$

where: $A = R_s^2 + \omega_s^2 L_s^2$, $B = 2R_s\omega_s M^2/L_r$ and $C = R_s^2 + \omega_s^2\sigma^2 L_s^2$.

This voltage-limit boundary, given by (19), is an ellipse, which area and angle of major axis depend on voltage and frequency. Equation (17) in the same axis system explains a circle, so range of drive operation can be found in cross section of these two ones.

In voltage dip case, based on (19), new ellipse can be drawn responding to the reduced voltage limit, where is easily noticeable decreasing of maximum possible *q*-axis stator current component which corresponds to electrical torque reduction. In this case, for constant load torque, this leads to the speed regulation loss, which explicitly explains if we build adequate torque-speed characteristics. Figure 6 shows the curves that correspond to these limits, and also drawn the trajectory of constant rotor flux and constant stator flux, which illustrates the ASDs working point with RFO and DTC control algorithm, respectively. Intersection among flux trajectories and contours that correspond to voltage and current limit restrictions give concrete electric motor drives torque/speed behaviour, depending on the applied control algorithm. Obvious fact is that RFO and DTC drive control differenceses can lead to various torque limits during voltage sag conditions.

Figure 7 shows these differences for the case of average voltage reduction to 80% of nominal which corresponds to the worst case situation of dc link voltage reduction (C type voltage sag with h=0.333) and, additionally, we have a significant second harmonic occurrence at same time. It should be noted the fact that adjusting

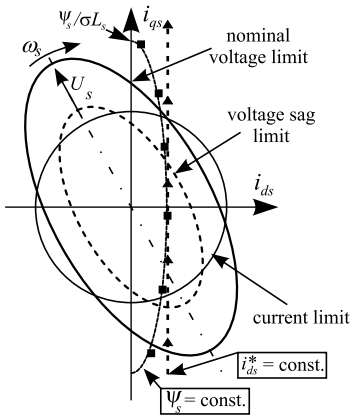

Fig. 6. Voltage and current limits under nominal and voltage sag conditions.

the value of flux allows the correction of the maximum available torque and in some cases overcome the consequences of voltage sag. More detailed analysis regarding voltage reduction effects and several possibilities for ride through are given in [9].

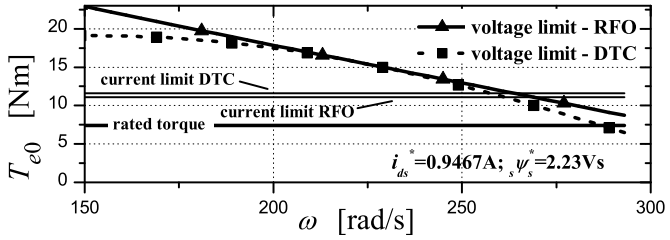

Fig. 7. Maximum torque comparison for $V_{DC} = 80\%V_{DCn}$ for RFO controlled and DTC drives.

4.2 DC link voltage ripple effects

The presence of second harmonic in dc link voltage, as shown in equation (16), leads to appearance of additional harmonic torque, which can cause vibration and motor overheating. It should be noted the fact that the dominant, side harmonic T_{e2} depends on the output frequency and motor load which is shown in Fig. 8 (based on formula (16)).

In the case of ASDs with the RFO and DTC control, expected behaviour is significantly different. It is well known that RFO vector control has two internal, fast control loops for i_{ds} and i_{qs} currents. From the aspect of current control loops oscillatory components i_{qs2} and i_{ds2} represent external disturbances such as it is

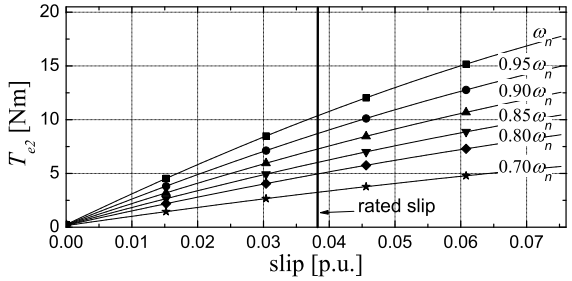

Fig. 8. Slip and output frequency influence on torque.

shown in Fig. 9 in continuous time domain, neglecting the sample and hold effects.

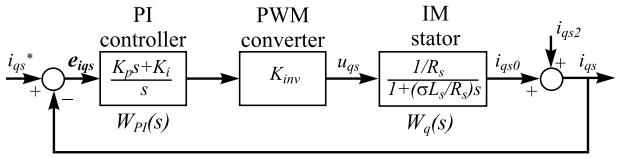

Fig. 9. RFO controlled drives q-axis current control loop.

The design of PI controller is made to cancel the machine pole $K_i/K_p = R_s/\sigma L_s$, and if a desired system bandwidth of ω_{bw} is defined, the proportional and integral gains are ([10]):

$$K_p = \sigma L_s \omega_{bw}, \text{ and} \tag{19}$$

$$K_i = R_s \omega_{bw}. \tag{20}$$

Error signal in control loop, shown in Fig. 9, can be represented as:

$$e_{iqs} = e_{ir} + e_{id} \tag{21}$$

where the e_{ir} indicates an error in tracking the reference signal $i_{qs}*$; e_{id} marks the error arising from effects of the disturbance, calculated as:

$$e_{id} = -W_{i2}(s) i_{qs2} = -\frac{1}{1+W_{PI}(s)W_q(s)} i_{qs2} \tag{22}$$

For a PI controller, whose parameters are given in (20) and (21), Bode diagram of function W_{i2}(s) is shown in Fig. 10. Increasing bandwidth of PI controller directly influence to the reduction of current amplitude oscillations while retaining basic frequency $2\omega_i$ in currents $i_{qs}(t)$ and $i_{ds}(t)$. Increasing bandwidth is necessarily

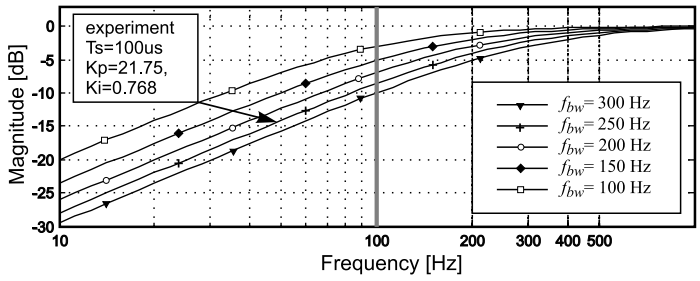

Fig. 10. Current loop bandwidth influence on second harmonic component.

accompanied by the request of increasing switching frequency, which is the limit imposed by the IGBT transistors. In the experiments, accomplished in the paper, current control loops bandwidth is set on 1250rad/s, which is mainly limited by noise presence in measured currents. For induction motor data, given in Table 2, digital PI controller parameters for *d* and *q* current control loops are K_p=21.75 and K_i=0.768 when sample time is set to 100μs.

Table 2. Motor data (per phase) and ASD parameters.

Rated power / speed	2200W/2835rpm
Stator voltage U_s	230V
Stator resistance R_s	2.7Ω
Stator leakage inductance L_{ls}	10.5mH
Rotor resistance R_r	2.2Ω
Rotor leakage resistance L_{lr}	10.5mH
Mutual inductance M	270mH
Motor inertia J_m	0.00184kgm2
Total leakage coefficient σ	0.073
DC link capacitance (C_f)	2x330mF(in series)
DC link inductance (L_f)	2x3.6mH

In case of DTC control application, there are two control contours: one for stator flux regulation and the other one for torque control as a slave controller in speed control loop. Torque control structure shown in Figs. 4 and 5 are similar because in both exist a decoupled flux and torque control, and for simplicity of analysis can be considered that the C12DTC scheme derived from PIDTC control structure. Suitable torque control, in the case of constant stator flux, is achieved by setting voltage component u_{qs} in synchronous reference frame related to the stator flux. Torque control loop is shown in Fig. 11 together with the corresponding induction motor and PI controller transfer functions.

In this article, PI torque controller design was done using root loci method with the help of Matlab SISO tool (Control System Toolbox, [11]) entering natural frequency ω_n and coefficient of relative damping ratio ξ. Similarly to the analysis

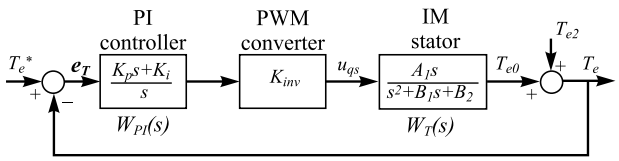

Fig. 11. Torque control loop in PI-DTC drives.

for RFO electric drive, influence parameters of PI controller on disturbance error analysis can be explored using Bode plot diagram of function W_{T2} given by the relation:

$$e_{Td} = -W_{T2}(s)T_{e2} = -\frac{1}{1+W_{PI}(s)W_T(s)}T_{e2}. \tag{23}$$

The coefficients of transfer function $W_T(s)$ are terms of:

$$A_1 = \frac{1.5\psi_s}{\sigma L_s}; B_1 = \frac{R_s L_r + R_r L_s}{\sigma L_s L_r}; B_2 = \frac{1.5\psi_s}{\sigma L_s J_m}. \tag{24}$$

Setting parameter values natural frequency w_n in the range from (2π100) rad/s to (2π300) rad/s, and with fixed setting ξ=0.707, Bode diagram of $W_{T2}(s)$ are drawn in Fig. 12. Having in mind the existence of induction motor parameters uncertainty and control algorithm implementation in digital form, the experiment proved that the optimal settings of parameters regulator are: K_{pT}=19.875 and K_{iT} =0.425, for torque; and $K_{p\psi}$=2500 and $K_{i\psi}$=0.425 for flux. For these controller parameters in Fig. 12 amplitude/frequency characteristic is drawn.

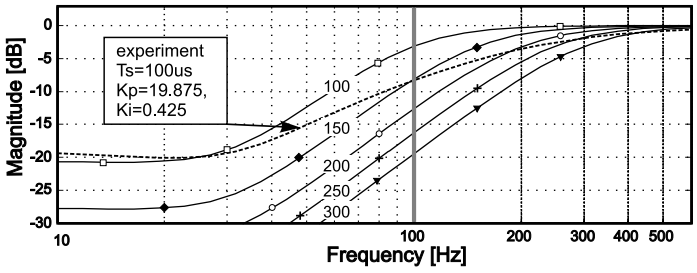

Fig. 12. PI controller adjusting influence on torque ripple.

In the case of classical DTC with the torque (flux), hysteresis controller, whose bandwidth is infinite (practically restricted by power transistor switching speed), it is clear that the reduction of side harmonic components is almost completely, which explains the experimental results obtained later.

5 Experimental Results

The test bed used for testing of ASDs consisted of the following main parts:

1. Rapid prototyping system based on dSpace DS1104 and with modified industrial frequency converter Danfoss VLT5003.
2. Voltage sag generator consisting of three-phase power transformer with interchangeable vector group (Dy, Yd or Yy) and with one autotransformer on primary side and switch network controlled by PLC [12]. Maximum output power is 15kVA.
3. Independent real-time data acquisition system (LMG450 Multi Channel Power Analyzer) with four current and four voltage inputs and with 0.1% basic accuracy.
4. Loading induction motor with servo controller interfaced to dSpace DS1104.
5. Vibration measurement instrument VIBROTEST 60 with piezo-electric acceleration sensor AS-065 [13].

The first set of experiments was performed with a V/Hz ASD, controlling a motor loaded in steady state by a constant torque of 7Nm at rotational speed of 240rad/s. Shortly after the B sag (h=0) initiation, overcurrent protection was activated. In order to observe changes in relevant ASD/motor parameters without tripping the drive, motor load was reduced to 6Nm. Figure 13 presents the effects of a single-phase type B voltage sag, obtained in experimental measurements. It can be seen that the presence of large ripples in both dc link voltage and torque (with dominant second harmonic) identified in theoretical analysis, which is also confirmed in experiments.

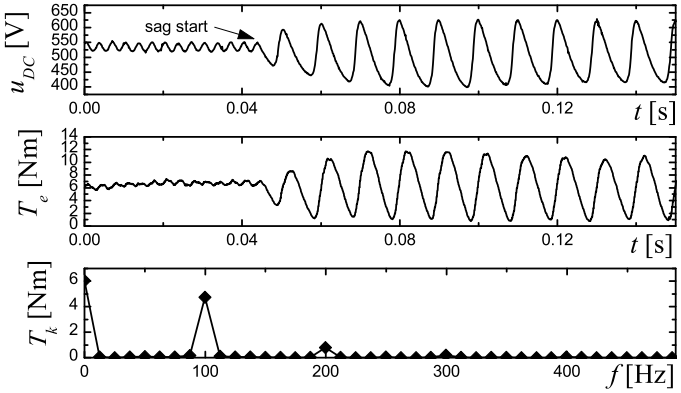

Fig. 13. B type voltage sag effects on V/Hz drive.

Afterwards, the RFO drive was tested with nearly the same rotational speed, but with the load torque equal to the rated one (7.4Nm). At time t=0.04s voltage sag was initiated. Figure 14 presents measurement results, where a significant reduction in torque ripple is evident in comparison to V/Hz controlled drive. It can be also seen that the characteristic torque harmonics occur at the same frequencies for RFO drive as for V/Hz drive, but the magnitude of the dominant 100Hz component is significantly smaller in the case of RFO drive.

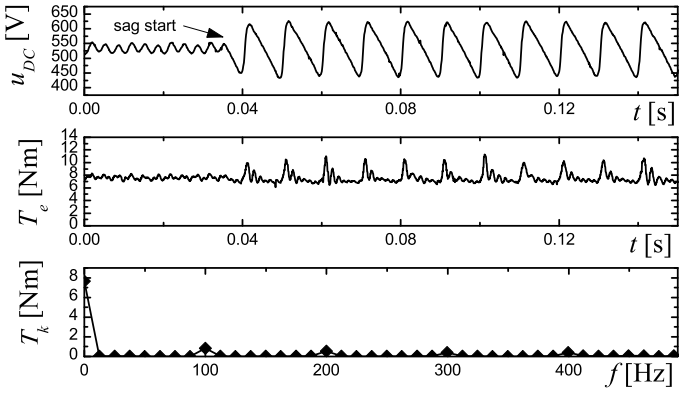

Fig. 14. B type voltage sag effects on RFO drive.

DTC drives with PI controllers possess nearly the same torque closed loop bandwidth as well as RFO drives at torque producing current components control loop (See note in Fig. 12). Expectations regarding the torque harmonics, at the same condition as RFO drives, are reached in Fig. 15: reduction was almost three times, which corresponds to the theoretical results from Fig. 12. Twelve sectors DTC drive is submitted to voltage unbalance and in Fig. 16 can be seen the expected dc bus voltage ripple, but at the estimated torque practically is not visible voltage sag influence. Torque control loop with hysteresis controller efficiently suppresses torque oscillation that is illustrated in the importance in achieving torque recall as fast as possible.

In addition, the torque harmonic spectrum is shown in the Figs. 13-16 as a confirmation of the theoretical analysis carried out. Additional measurements of ASDs vibration can also confirm the previous results (torque harmonic spectrum) and may indicate the possibility of interaction between sag-caused vibrations with purely mechanically induced vibrations at inter-harmonic frequencies.

In Fig. 17 are presented alongside measured vibration spectra for these adjustable-speed drives. Under normal supply operation, in Fig. 17.a) can be noticed vibrations that match the rotation frequency (approximately 40Hz). Vibration harmonics

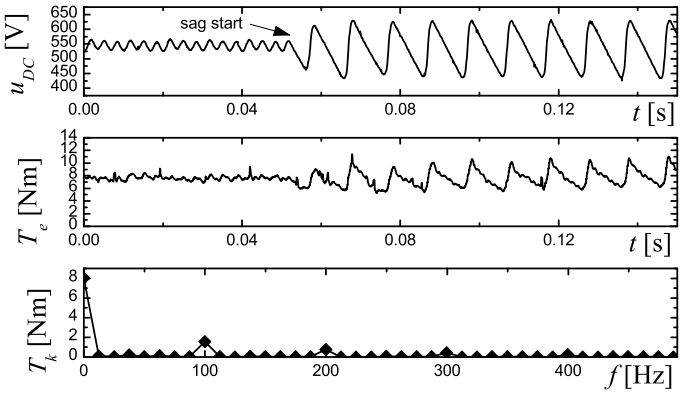

Fig. 15. B type voltage sag effects on PI-DTC drive.

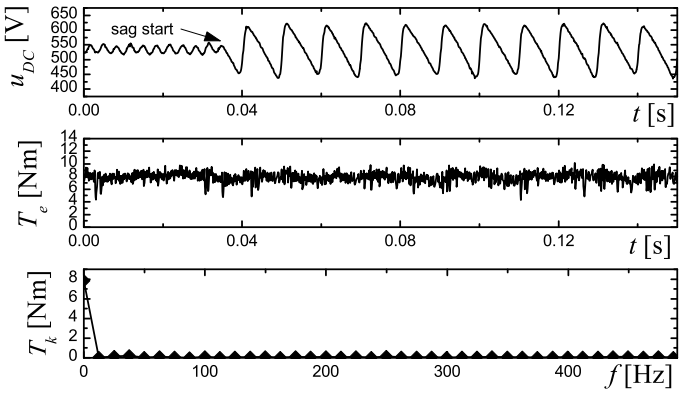

Fig. 16. B type voltage sag effects on C12DTC drive.

at frequencies $k\times$40Hz (k=1, 2, ...) are the consequences of non-perfect mechanical construction (motor and load coupling misalignment). Component with 100Hz frequency is direct consequence of the voltage sag. Interharmonics, which are the consequence of the inter-reaction between vibration mechanical components (at $k\times$40Hz) and sag component at 100Hz can also be seen. In the case of ASDs with a scalar control (Fig. 17.b) can be observed a significant amplitude of the vibration at power supply second harmonic frequency and aside vibration harmonics at 140Hz and 180Hz (interharmonics).

Reduction of torque oscillations for RFO ASD are also confirmed in vibration measurements (Fig. 17.c), where again sag-caused vibrations occur at previously identified frequency, but now with significant amplitude reduction. As PIDTC drive has almost the same bandwidth for torque closed loop as the RFO drive for torque-

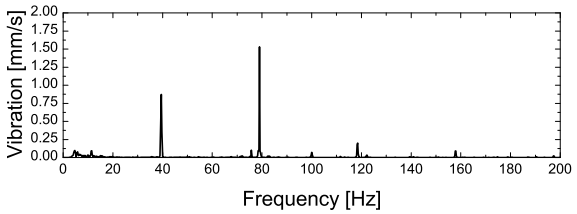

a) *normal supply operation*

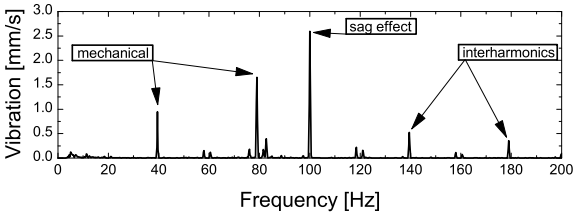

b) *V/Hz drive with B type sag (h=0)*

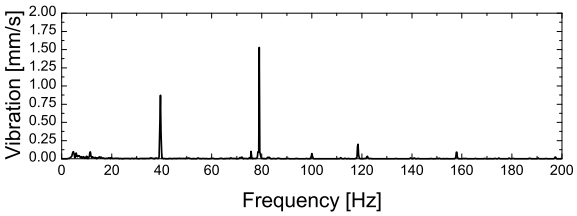

c) *RFO drive with B type sag (h=0)*

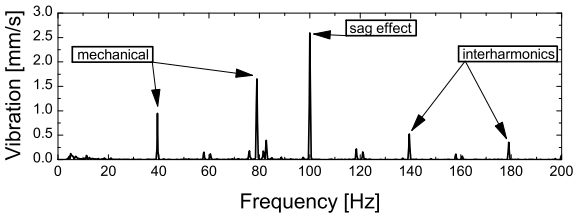

d) *PIDTC drive with B type sag (h=0)*

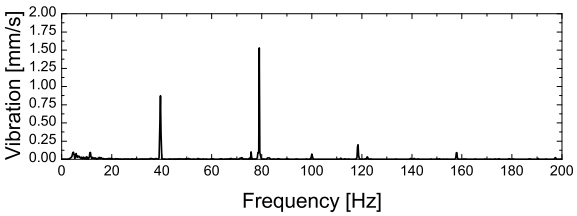

e) *C12DTC drive with B type sag (h=0)*

Fig. 17. ASDs vibration spectra

producing current components control loop, the corresponding vibration measuring results are similar (Fig. 17.d). In both cases the reduction of dominant, sag-casused vibration is almost 4.5 times, while the appearance of additional interharmonics almost negligible.

Finally, the measurement of vibration in the case of C12DTC drives confirmed the analytical results expected in the presence of vibration amplitude and harmonic values. In the area of low frequency vibration spectra, in Fig. 17.e) can be seen only harmonics that are a consequence of the rotation, while the vibrations are a result of voltage sag completely suppressed.

6 Conclusion

Modern adjustable speed drives, regarding to voltage sag condition, have different characteristics, in terms of momentary tripping or partial performance degradation. This paper, based on analytical expressions, predicts the behaviour of induction motor drives in case of SLGFs caused voltage sags, and then, respecting the different control algorithms allows assessment torque/speed behaviour of high performance drives. Based on analytical expression and experimental researches, we conclude that type control algorithm is with great importance considering unsymmetrical sag effects.

High performance drives (with RFO and DTC algorithm) are less sensible on voltage unbalance, especially drives with traditional DTC technique with hysteresis comparators. Torque or torque-producing current clossed-loop bandwidth is a key parameter with the greatest influence on the amplitude of unwanted harmonics. Experimental measurements in industrial ASDs in which they implemented various control algorithms confirmed the theoretically predicted results. Laboratory measurements indicated the potential risk of inter-reaction between vibration mechanical components and sag-caused torque component, which as a result can be appearance of inter-harmonics whose frequency can be found in the area of natural system resonance, especially for drives in a wide speed range.

Professional engineers in the field of industrial electric drives can be in the stage of plant system design choose a lower operating speed, which will significantly reduce possible oscillation in torque. In addition, the application of advanced control methods, particularly traditional DTC technique, is one of the possibilities for overcoming the voltage sag consequences and prevents degradation of ASDs performance. Further researches will be conducted on the disturbance observer application in torque/current control loops aimed to additional torque harmonics suppression.

References

[1] S. Djokić, K. Stockman, J. Milanović, J. Desmet, and R. Belmans, "Sensitivity of ac adjustable speed drives to voltage sags and short interruptions," *IEEE Trans. Power Delivery*, vol. 20, pp. 494–505, Jan. 2005.

[2] M. H. J. Bollen, *Understanding power quality problems: Voltage sags and interruption*. New York, USA: IEEE Press series on Pwr. Engineering, 2000.

[3] D. Divan, G. Luckjiff, W. Brumsickle, J. Freeborg, and Bhadkamkar, "I-grid^{TM}: infrastructure for nationwide real-time power monitoring," in *Industry Applications Conference, 2002. 37th IAS Annual Meeting. Conference Record of the*, Philadelphia, Pennsylvania, Oct. 2002, pp. 1740–1745.

[4] K. Lee, T. Jahns, W. Berkopec, and T. Lipo, "Closed-form analysis of adjustable-speed drive performance under input-voltage unbalance and sag conditions," *Industry Applications, IEEE Transactions on*, vol. 42, no. 3, pp. 733–741, May-June 2006.

[5] M. P. Kazimierkowski, F. Blaabjerg, and R. Krishnan, *Control in Power Electronics – Selected problems*. New York, USA: Academic Press, 2002.

[6] N. Nash, "Direct torque control, induction motor vector control without an encoder," *IEEE Trans. Ind. Appl.*, vol. 33, no. 2, pp. 333–341, Mar. 1997.

[7] V. Kostic, N. Mitrovic, M. Petronijevic, and B. Jeftenic, "Torque ripple minimization in direct torque controlled induction motor drive based on duty ratio modulation method," *Scientific Bulletin of "Politehnica", Trans. on Automatic Control and Computer Science*, vol. 49(63), no. 1, pp. 87–92, 2004.

[8] Y. Lai and J. Chen, "A new approch to direct torque control of induction motor drives for constant inverter switching frequency and torque ripple reduction," *IEEE Trans. On Energy Conversion*, vol. 16, no. 3, pp. 220–227, Sept. 2001.

[9] M. Petronijevic, B. Jeftenic, N. Mitrovic, and V. Kostic, "Voltage sag drop in speed minimization in modern adjustable speed drives," in *Proceedings of the IEEE International Symposium ISIE*, vol. 3, Dubrovnik, Croatia, June 2005, pp. 929–934.

[10] D. Telford, M. W. Dunnigan, and B. W. Williams, "Online identification of induction machine electrical parameters for vector control loop tuning," *IEEE Trans. Ind. Electron.*, vol. 50, no. 2, pp. 253–261, Apr. 2003.

[11] F. Blaabjerg, M. Kazmierkowski, M. Zelecehowski, D. Swierczynski, and W. Kolomyjski, "Design and comparison direct torque control techniques for induction motors," in *Proceedings of European Conference on Power Electronics and Applications*, Dresden, Germany, Jan. 2005, pp. 253–261.

[12] M. L. Rockfield, P. S. Tejindar, and C. B. Siddharth, "Non-rotating portable voltage sag generator," EPRI, Tech. Rep. Patent 5920132, July 1999. [Online]. Available: http://www.freepatentsonline.com/5920132.html

[13] *Vibrotest 60 User manual*, Bruel and Kjaer Vibro, Danmark, 2007.